# The Evolution of Carbon Nanotube Network Structure in Unidirectional Nanocomposites Resolved by Quantitative Electron Tomography

Bharath Natarajan,[†,§,#] Noa Lachman,[‡,#] Thomas Lam,[†] Douglas Jacobs,[||] Christian Long,[†,§] Minhua Zhao,[†,⊥] Brian L. Wardle,[‡] Renu Sharma,[†] and J. Alexander Liddle*,[†]

[†]Center for Nanoscale Science and Technology, National Institute of Standards and Technology, Gaithersburg, Maryland 20899, United States, [§]Maryland Nanocenter, University of Maryland, College Park, Maryland 20740, United States, [‡]Department of Aeronautics and Astronautics, Massachusetts Institute of Technology, Cambridge, Massachusetts 02139, United States, [||]Department of Mechanical Engineering, Massachusetts Institute of Technology, Cambridge, Massachusetts 02139, United States, and [⊥]Department of Materials Science & Engineering, University of Maryland, College Park, Maryland 20740, United States. [#]These authors contributed equally.

ABSTRACT Carbon nanotube (CNT) reinforced polymers are next-generation, high-performance, multifunctional materials with a wide array of promising applications. The successful introduction of such materials is hampered by the lack of a quantitative understanding of process—structure—property relationships. These relationships can be developed only through the detailed characterization of the nanoscale reinforcement morphology within the embedding medium. Here, we reveal the three-dimensional (3D) nanoscale morphology of high volume

3D Reconstruction Network Structure Degree of Alignment

fraction (V_f) aligned CNT/epoxy-matrix nanocomposites using energy-filtered electron tomography. We present an automated phase-identification method for fast, accurate, representative rendering of the CNT spatial arrangement in these low-contrast bimaterial systems. The resulting nanometer-scale visualizations provide quantitative information on the evolution of CNT morphology and dispersion state with increasing V_f, including network structure, CNT alignment, bundling and waviness. The CNTs are observed to exhibit a nonlinear increase in bundling and alignment and a decrease in waviness as a function of increasing V_f. Our findings explain previously observed discrepancies between the modeled and measured trends in bulk mechanical, electrical and thermal properties. The techniques we have developed for morphological quantitation are applicable to many low-contrast material systems.
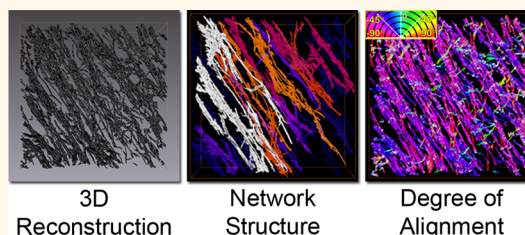
KEYWORDS: electron tomography · carbon nanotubes · nanocomposites · image analysis · nanostructure

Nanocomposites are the subject of sustained and increasing interest because of their potential not only to provide tunable multifunctional properties,[1,2] but also because they may do so in readily processable forms.[3] This latter factor will dramatically lower manufacturing costs, and enable their deployment in a broad range of consumer products. For this potential to be realized, however, it is essential to establish a fundamental understanding of process—structure—property relationships.

The attractive intrinsic axial properties of carbon nanotubes (CNTs) have motivated numerous research endeavors focused on controllably fabricating "ideal", aligned-CNT (A-CNT) nanocomposites with impressive

multifunctional properties.[4-6] The novel processing methodologies developed through these efforts have resulted in a catalogue of A-CNT composite structures such as ribbons,[7] fibers,[8] aligned bucky papers[9] and bulk materials[10] targeted toward various applications, e.g., mechanical reinforcement in hierarchical materials,[11,12] thermal management (thermal interfaces, heaters),[13,14] energy storage,[5,15] drug/fluid transport membranes,[16] etc.

We have previously reported a biaxial mechanical densification approach for fabricating ultrahigh volume fraction (V_f) A-CNT epoxy nanocomposites with excellent control over CNT loading and dispersion.[10] These nanocomposites have shown electrical, mechanical, and thermal properties

in the direction of CNT alignment that are far superior to those of randomly dispersed-CNT nanocomposites.[6,17] The electrical and thermal conductivities, in particular, are some of the highest reported for nanocomposite materials.[6,17] However, these studies also find that the measured properties do not increase linearly as a function of V_f, as would be predicted by effective medium calculations for perfectly aligned, straight, noninteracting, nondefective, CNT structures. This mismatch has been hypothesized to be due to morphological deviations from the ideal structure and their evolution with varying V_f.[17,18] These deviations may take the form of (a) bundling, which can lead to an increased engagement of nanotubes in conduction with increasing V_f; (b) misalignment, which leads to a reduction in the degree of anisotropy; (c) structural defects in the CNT walls, which act as scattering sites impeding conduction; and (d) the inherent and processing-induced waviness of nanotubes, which is known to lead to a decrease in elastic modulus.[18,19] The differences between expected and actual values of V_f due to processing artifacts such as shrinkage or expansion during matrix infiltration and curing exacerbate this mismatch.[20,21] Therefore, a quantitative understanding of the nanoscale structure is needed to build accurate, validated models that relate processing to structure and thence to properties. However, detailed quantitative characterization of the morphology is thus far lacking. 2D imaging techniques (scanning electron microscopy (SEM), transmission electron microscopy (TEM) projections) are of limited use in extracting the complex 3D structure of the embedded CNTs.[22] Complementary scattering methods have revealed details about the alignment of the embedded CNTs, but they do not provide information on bundling or tube–tube contacts.[10] Conventional mass-fraction-based techniques such as thermogravimetric analysis are not well suited to measuring the V_f, due to the chemical similarity of the matrix and filler phases (carbon in carbon).[23] This is further complicated by uncertainties involved in determining CNT density.[24]

These limitations can be overcome by electron tomography which is rapidly becoming the preferred method for nanoscale 3D structural analysis.[25,26] In tomography, a series of projections is obtained at different tilt angles and reconstructed into a 3D image using mathematical algorithms. The reconstructions then undergo a process of segmentation, in which gray levels are assigned to the phase(s) of interest. Segmentation is followed by visualization and analysis of the labeled phase(s). Previous efforts to study bimaterial composites by electron tomography have been focused on systems with aggregated inorganic fillers, which show excellent contrast in the (Scanning) TEM when embedded in an organic matrix.[27−30] These aggregated systems do not require high-resolution tomography and the images obtained have primarily been used for qualitative purposes.

Here, we demonstrate the use of 3D electron tomography for accurate, quantitative, morphological characterization of aligned CNT nanocomposites having volume fractions that vary over an order of magnitude. The high-resolution visualizations thus obtained are used to quantify V_f, degree of alignment and waviness, network and bundle structure. This quantification protocol is a first step toward establishing structure–property relationships in these important material systems. The results contained herein also validate the hypothesis proposed to explain the nonlinear scaling between volume fraction of CNTs and various bulk properties,[17] and provide quantitative data that enable the construction of predictive models.

Aligned nanocomposites, containing CNTs with an average diameter of about 8 nm, were prepared by biaxial densification as described briefly in the Methods section and in more detail elsewhere.[6] The values of V_f (which serve henceforth as the sample identifiers) were 0.44%, 2.6%, 4%, and 6.9%. We use focused ion beam (FIB) milling in a Dual-Beam FIB/SEM tool to prepare lamellar electron-transparent (200 nm thick) TEM samples (Supporting Information Figure S1c). Charge-contrast SEM images are used to verify that the CNTs are aligned in the plane of the TEM lamellae, parallel to the tilt axis (Supporting Information Figure S1a,b).[31] Simulations show this to be the orientation best suited for the optimal interpretation and reconstruction of aligned tubular structures.[32] The TEM samples thus prepared are coated with a low concentration of 5 nm gold particles (smaller than the CNT diameter) that serve as fiducial markers for alignment during tilt series acquisition (Supporting Information Figure S1d). Further details of sample preparation can be found in the Methods section.
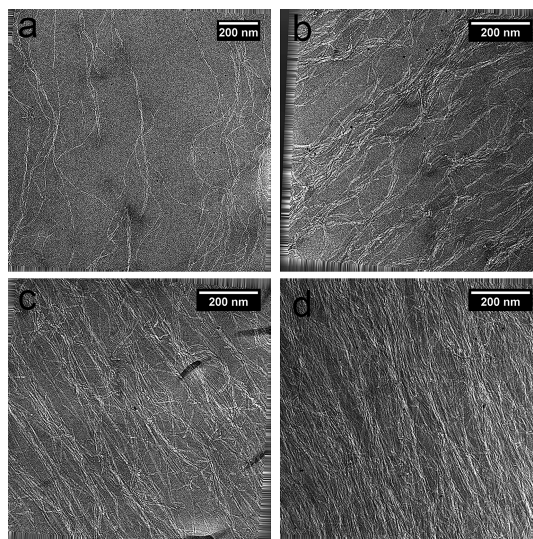

Figure 1. Representative 0° tilt energy-filtered (10 eV window around 0 eV) BF-TEM images of A-CNT nanocomposites with V_f of (a) 0.44%, (b) 2.6%, (c) 4%, and (d) 6.9%.
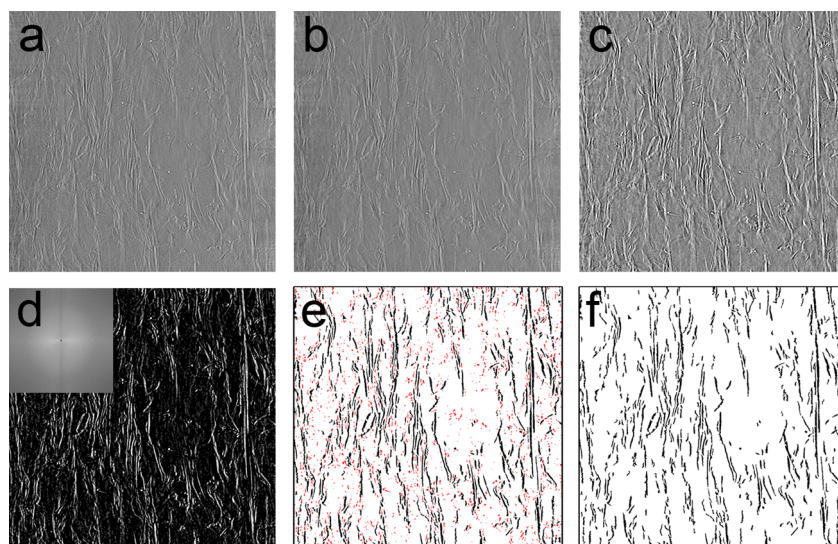
Figure 2. Stages of image stack segmentation prior to visualization: (a) representative orthoslice (877 nm × 857 nm) from image stack (V_f of 6.9%); (b) anisotropic diffusion smoothing applied to (a); (c) bandpass filter applied to (b); (d) inverse FFT of masked power spectrum of (c) (inset); (e) thresholding and binarization applied to (d) with noise artifacts shown in red; (f) image (e) with noise artifacts subtracted.

The ratio of inelastically scattered to elastically scattered transmitted electrons is high for low atomic number elements such as carbon.[33] Such materials cause a significant energy spread in the electron beam, leading to a degradation of image contrast due to chromatic aberration and a large background noise. Carbon nanostructures such as CNTs are therefore typically found to have poor contrast *versus* a carbonaceous matrix in conventional bright-field TEM (BFTEM).[31] Segmentation is thus difficult since unambiguous identification of gray levels corresponding to the CNTs alone becomes nearly impossible. We mitigate this problem by eliminating most of the inelastically scattered electrons by using a 10 eV wide energy filter centered about the zero-loss peak.[34,35] This filtering enhances the contrast arising from density variations between the CNTs and the polymer matrix, and enables imaging through thicker sections at higher tilts.[33,34] The hollow CNTs therefore appear as bright cylindrical structures in an amorphous, noisy epoxy background (Figure 1).

The tilt series, obtained between −60° and +60°, is aligned to a common origin and tilt axis by bead tracking of the gold nanoparticles to within subpixel accuracy and is then reconstructed using the simultaneous iterative reconstruction technique (SIRT).[36] This results in a 3D volume comprising 1-pixel thick 2D slices (*XY* planes) stacked along the direction of the electron beam (*Z*). Simulations of model nanocomposite structures with poor contrast show SIRT to be the most robust method, with little dependence on imaging conditions, even at low doses, and the tilt angles used.[36] SIRT is therefore well-suited for electron beam-sensitive carbon nanostructure/polymer materials. The imaging and reconstruction are described in further

detail in the Methods section and Supporting Information, respectively. We find that the low signal-to-noise ratio of the unsegmented reconstructions produced using SIRT prohibits the use of standard automated segmentation techniques such as thresholding and watershed algorithms. Manual segmentation, the most commonly used method,[37] is subjective, but has been found to yield reasonably accurate V_f measurements;[38] however, it is extremely time-consuming. There is thus a pressing need for new segmentation techniques that will enable the quantitative analysis of statistically significant data sets.

To address this need, we have developed an algorithm that performs accurate, unbiased segmentation of reconstructions approximately 50 times faster than manual segmentation, thus enabling the analysis of larger, more representative volumes. Our algorithm can be implemented easily on open-source software such as ImageJ[39] and is well-suited for other low-contrast systems such as fuzzy fiber CNT or nanocellulose polymer composites. Figure 2 shows the segmentation steps applied to a representative slice (0.43 nm thick) of the 6.9% V_f sample. An "anisotropic diffusion" (Perona-Malik diffusion) smoothing is first applied to the slice in order to reduce image noise (Figure 2b). This smoothing technique preserves edges, lines and finer details important for image interpretation.[40] A bandpass filter (BPF) is then applied to the smoothed image to remove lower frequency variations associated with sample thickness nonuniformity and to remove high-frequency variations associated with Poisson (shot) noise (Figure 2c). The BPF also aids in suppressing the horizontal stripes along the edges that arise from reconstruction. Next, a fast Fourier transform (FFT) of the BPF image is obtained and an appropriate

high-pass mask is applied to the power spectrum (inset, Figure 2d). The mask eliminates average brightness information and the low frequency background. The inverse FFT of the masked power spectrum reveals bright CNTs against a dark background (Figure 2d). This image is then thresholded to a level which maintains the CNT diameter as determined from actual projections (Figure 2e) and HRTEM images (Supporting Information Figure S4). This thresholding protocol is expected to produce more realistic reconstructions by minimizing errors that arise from subjective binarization.[41] Thresholding also ensures that only the brightest regions, corresponding to in-focus CNTs, are segmented and the less-sharp, out-of-focus regions corresponding to "missing wedge" artifacts are, to a large part, eliminated.[25] The remaining noise in the image appears as nearly circular artifacts. They are isolated by size (units of pixels^2) and circularity-based masking and eliminated using image subtraction (Figure 2f). A 3D Gaussian smoothing ($\sigma = 1$ pixel) is applied to stack of segmented images to eliminate regions that do not extend beyond a single slice. Larger noise artifacts are eliminated by volume-based thresholding of the smoothed stack. The stack thus segmented is ready for visualization and morphological analysis.

Representative visualizations for the different V_f samples are shown in Figure 3. The visualizations are found to match well with the original tilt series (compare Figure 1 and 3) and have a resolution of 1.8 nm. The a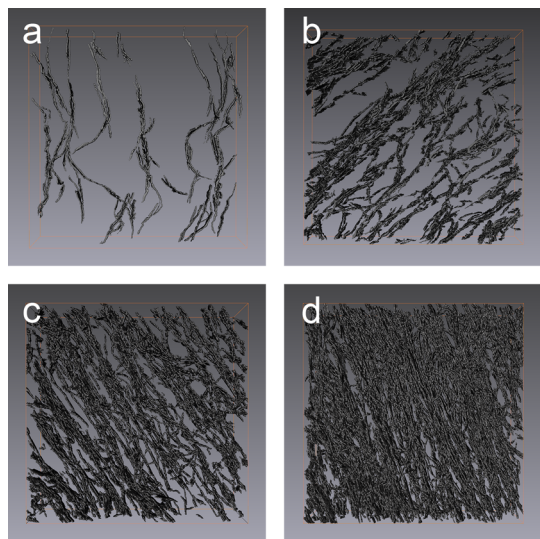verage outer diameter of the CNTs in the segmented 3D volumes is calculated to be (7.65 ± 0.87) nm (mean ± one standard deviation). This variation in diameter corresponds to CNTs having from 4 to 9 walls, assuming a CNT inner diameter of 5 nm. The measurement uncertainty is ±0.43 nm (±1 pixel), and is thus substantially less than the observed diameter variation. The average diameter and diameter variation are in good agreement with the 2D High Resolution TEM measurements made by us (Supporting Information Figure S4) and others previously.[10]

RESULTS AND DISCUSSION

The V_f is calculated as the ratio of the number of foreground (CNT) pixels to the total number of pixels in the volume. The values of V_f are found to be similar to those calculated by manual segmentation (Supporting Information Figure S5), confirming that our rapid segmentation technique is as accurate as manual segmentation. Due to the limited range of angles used, the reconstructions display artifacts arising from the "missing wedge" of data when using SIRT.[42] This missing wedge of information degrades the resolution along the optic axis (Z), leading to an elongation of features in the beam direction.[42] The elongation causes the CNT cross section to assume an elliptical shape, since the CNTs lie perpendicular to the beam. However, the resolution in the plane perpendicular to the beam (XY) is preserved. Since CNTs generally have a circular cross section, the elongation factor (e_z) can be calculated as the ratio of the major axis (XZ diameter) to the minor axis (XY diameter) of the elliptical cross section. The average elongation factor for each V_f, measured from isolated CNTs, is displayed in Table 1. These values are found to be similar to those previously predicted for this range of tilt angles.[43] Since elongation also leads to an increase in the apparent V_f, a correction factor of $1/e_z$ is applied to recover the "measured" V_f of the samples. The values of average "measured" V_f are shown in Table 1. This represents the first report of a direct method for V_f estimation of CNTs in these state-of-the-art aligned CNT nanocomposites. We note that other methods that calculate the volume fraction based on the weight fraction lack this level of accuracy. The errors that arise out of uncertainties in the CNT density (sensitive to diameter and number of walls)[24] are larger than those presented by the missing wedge, which can be quantified and employed for correction.

The changes in material properties are intimately linked to the evolution of the CNT morphology with V_f.[17] As the CNTs are brought closer together, short-range van der Waals attractions cause CNTs to bundle on different length scales.[44] Understanding the size and morphology of the bundles is, therefore, crucial to the interpretation of transport property measurements, and to the understanding of mechanical property enhancements, which depend strongly on

Figure 3. Volume-rendered reconstructions of (a) 0.44%, (b) 2.6%, (c) 4%, and (d) 6.9% V_f A-CNT nanocomposites obtained from sample volumes shown in Figure 1. The size of reconstructed volumes are (a) 1327 nm × 1349 nm × 320 nm, (b) 859 nm × 840 nm × 152 nm, (c) 854 nm × 848 nm × 220 nm, and (d) 840 nm × 840 nm × 199 nm. These volumes are designed to be representative by selecting regions that are orders of magnitude larger than the critical microstructural dimensions (CNT diameter and average CNT spacing). Note that a larger volume is probed for the 0.44% V_f sample since the CNT spacings are larger.

TABLE 1. Values of Average Uncorrected V_f, Elongation Factors, Measured V_f, Largest Network V_f, Largest Network V_f Percentages, Concentrations of CNT–CNT Contacts and Average CNT Segment Arc Length to Euclidean Distance Ratios of the 4 Different Samples Examined, Calculated from the Corresponding Values for 3 Randomly Selected, Reconstructed Regions per $V_f{}^a$

uncorrected CNT V_f (%)	elongation factor e_z	measured CNT V_f (%)	V_f of largest network (%)	V_f of largest network/ measured V_f (%)	concentration of CNT–CNT contacts (μm^{-3})	l/d
0.50 ± 0.01	1.12 ± 0.01	0.44 ± 0.01	0.061 ± 0.01	13.82 ± 1.68	$(7.2 ± 1.1) × 10^2$	1.28 ± 0.02
3.00 ± 0.28	1.16 ± 0.02	2.58 ± 0.25	0.28 ± 0.01	10.8 ± 0.42	$(1.5 ± 0.3) × 10^4$	1.27 ± 0.01
4.45 ± 0.21	1.11 ± 0.01	4.04 ± 0.19	0.55 ± 0.19	13.70 ± 4.8	$(2.1 ± 0.3) × 10^4$	1.24 ± 0.02
7.85 ± 0.50	1.14 ± 0.03	6.89 ± 0.43	3.20 ± 0.16	46.49 ± 2.28	$(5.4 ± 0.6) × 10^4$	1.21 ± 0.02

^{a} The uncertainties shown are standard deviations calculated from the values obtained from the 3 randomly selected reconstructed regions from each sample.
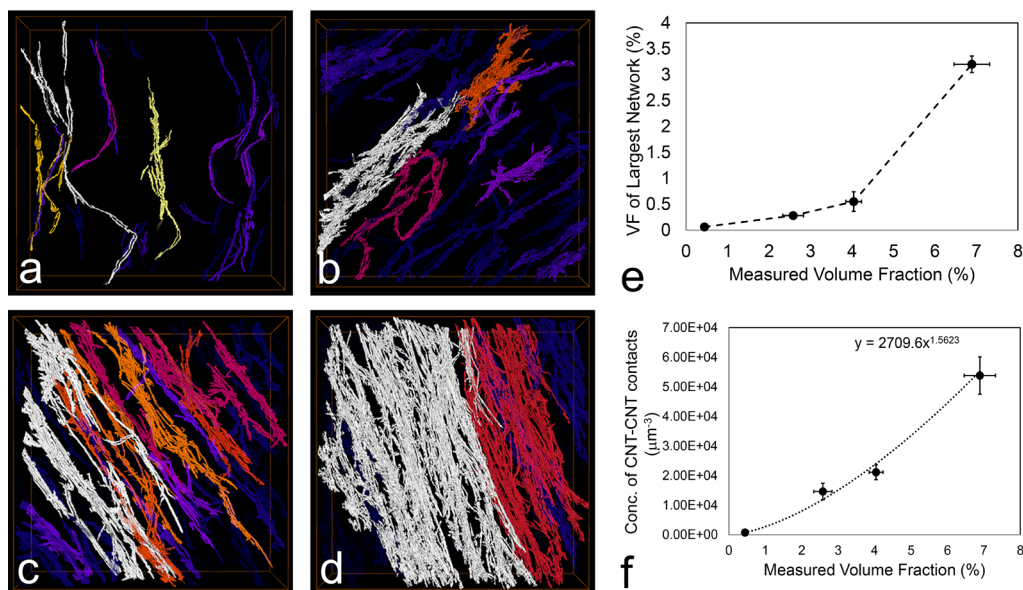

Figure 4. 3D network analysis of volume-rendered reconstructions of (a) 0.44%, (b) 2.6%, (c) 4.0%, and (d) 6.9% V_f of A-CNT nanocomposites obtained from sample volumes shown in Figure 1, with individual clusters identified by unique colors. The cluster in white represents the largest network in each rendered volume. (e) Plot of the V_f of the largest network *versus* the total measured V_f. The line serves to guide the eye. (f) Plot of the concentration of CNT–CNT contacts *versus* the measured V_f. The $X–Y$ uncertainties represent the standard deviation in values calculated from 3 randomly sampled volumes per V_f.

the amount of CNT–polymer interface available for stress transfer.[45] These bundles are identified in the segmented image stack by a multithreaded 3D object counting scheme (details in Supporting Information, **Figure S6**).[46] Connected regions are given color labels based on their calculated volumes. The stack is then color thresholded to isolate the bundled CNTs, as shown in Figure 4. The size of the bundles/connected domains increases with increasing V_f. The V_f of the largest network, which dominates electric and thermal conductivity, increases linearly with the increase in overall CNT V_f, up to 4% (Figure 4a–c). At higher CNT loading (6.9%, Figure 4d), most of the bundles are found to merge into a single large cluster containing nearly 50% of the total CNT volume.

This clustering is also expected to increase the number density of CNT–CNT contacts, resulting in more, and more continuous, high conductivity (electrical and thermal) pathways for charge carriers and phonons through the material. At sufficiently high values of V_f, CNT–CNT contact, as opposed to CNT–matrix contact,

will determine the material transport properties. To obtain a quantitative measure of the CNT–CNT contact concentration, we skeletonize the stack of clustered objects using the Skeletonize 3D plugin on ImageJ (Supporting Information Figure S7).[47] This structure is analyzed using Analyze Skeleton (ImageJ plugin),[47] which provides detailed branch information. When two or more connected CNTs are counted as one skeleton object, the other CNTs/CNT segments are registered as a branches. The number of branch points or points of CNT–CNT contact corresponding to branches larger than a threshold size (10 nm, eliminating skeletonization artifacts) is tallied. The number density of CNT–CNT contacts (μm^{-3}) is found to change nonlinearly with V_f, increasing by nearly 2 orders of magnitude for an order of magnitude increase in V_f (Figure 4f and Table 1). This trend has important implications for electrical and thermal transport in such nanofiber networks, as well as failure through and around these CNT bundles.

The degree of alignment is critical in determining the degree of anisotropy in the properties of aligned
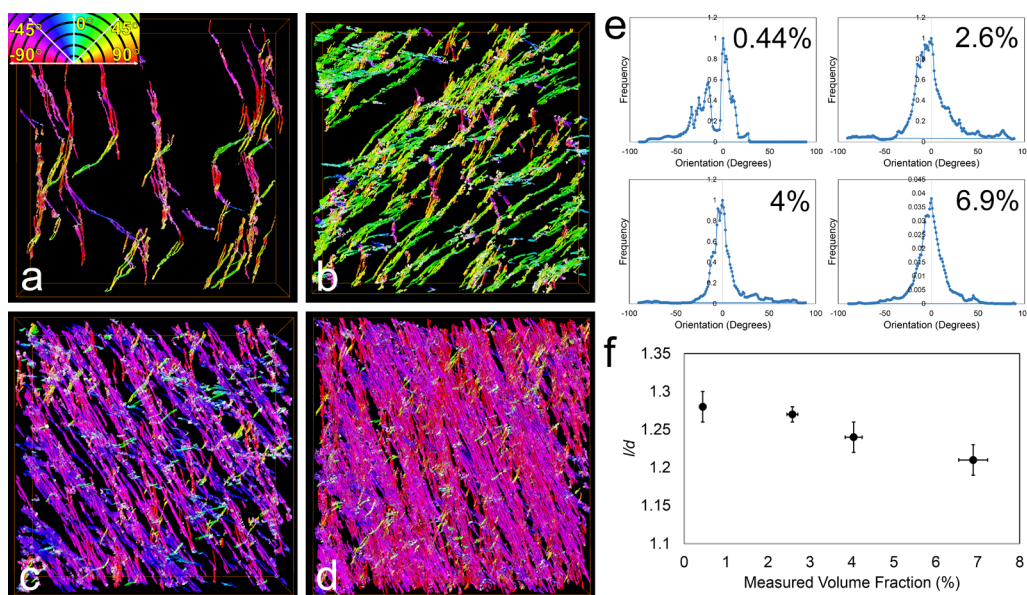
Figure 5. Orientation analysis of volume-rendered reconstructions of a) 0.44%, (b) 2.6%, (c) 4.0%, and (d) 6.9% V_f of A-CNT nanocomposites obtained from sample volumes shown in Figure 1. The NTs are color-coded according to the orientation color map from $-90°$ to $+90°$ shown in the inset in (a). The uniformity in color expresses uniformity in orientation, *i.e.*, alignment. (e) A plot of frequency *versus* the angle of orientation for the 4 different volumes shown in Figure 1. (f) A plot of the straightness *versus* the actual V_f ($l/d = 1$ is straight). The $X-Y$ uncertainties represent the standard deviation in values calculated from 3 randomly sampled volumes per V_f.

nanofiber based materials. Improved alignment is expected to lead to superior axial mechanical properties such as tensile modulus and strength, and increased anisotropy in transport properties. The orientation of the CNTs is evaluated by determining the structure tensors in the 2D image stack using OrientationJ, an ImageJ plugin.[48] Figure 5a−d shows the local CNT orientation, with angle mapped to color. A more uniformly colored image therefore represents a more aligned system. As can be seen, the degree of alignment improves with increasing V_f due to both the increased steric interactions between tubes and the increased level of bundling. This is also evident in the distribution plots, calculated from structure tensors (Figure 5e). These plots have been normalized by the peak frequency and peak-shifted to zero degrees, in order to enable a visual comparison of the distributions around the preferred alignment direction. At the lowest V_f, the angular distribution of fibers is broad. As the V_f increases, the peaks become sharper, with the angular range decreasing from $21°$ (1σ) at 0.44% to $10°$ at 6.9%. This trend is in qualitative agreement with small-angle X-ray scattering (SAXS) results reported earlier.[10]

Although a nonlinear morphological evolution in these systems with increasing V_f has been hypothesized to be responsible for the nonlinear improvements in electrical and thermal conductivities,[17] our results are the first observations that confirm this hypothesis. In the case of thermal conduction, for example, it has been reported that, even in aligned CNT arrays, not all CNTs participate in conduction through the sample thickness. This is attributed to variations in alignment and

continuity leading to a lack of engagement with the source and sink.[49] The bundling/clustering of CNTs that occurs at higher values of V_f means that a higher proportion of CNTs are contributing to conduction. The ratio of the volume of the largest cluster, as obtained from 3D Object analysis, to the overall CNT volume in the reconstruction is thus a quantitative measure of the availability of highly conductive paths (Table 1). In fact, the sharp increase in this ratio above a 4% V_f mirrors the trend in the thermal conductivity increase previously reported.[17] The thermal conductivity increase is further aided by the increases in alignment and CNT−CNT contact concentration.

It is now well established that the curvature of CNTs significantly reduces the anticipated increase in modulus in NT nanocomposites.[18,19,50] This curvature is represented through a parameter called "waviness", which is the ratio of the amplitude to the wavelength of a sine curve fit through a curved section of the tube. Micromechanical models, in agreement with experimental results, show that, for identical interphase properties, nanocomposite modulus diminishes with increasing waviness.[51] Waviness has been characterized only from 2D images so far. Here, we use the skeletonized volumes, containing only the line traces of the original tubes, to obtain the pixel coordinates corresponding to each CNT line in 3D. These coordinates are then used to extract the arc length (l) and the end to end/Euclidean distance (d) of individual CNT segments of length greater than 80 nm (an order of magnitude larger than the CNT diameter). The ratio of these parameters (l/d), the inverse of which, is

sometimes called the "straightness parameter", is an indirect measure of 3D waviness, with the waviness increasing with increasing l/d ($l/d = 1$ for a straight line, Supporting Information Figure S7). The average l/d value for each V_f is shown in Table 1. The l/d values can also be used to calculate the 2D waviness in its most commonly defined form (Supporting Information). The 2D waviness is found to decrease by 14% from 0.183 to 0.157 as the V_f increases from 0.44% to 6.9% (Figure 5f, Supporting Information Table S1). Recent results show that the axial elastic modulus becomes increasingly sensitive to waviness as the ratio of reinforcement to matrix moduli increases: in our case, $E_{CNT}/E_{epoxy} \approx 160$.[52] As a result, even the modest reduction in waviness that occurs as the CNTs become more closely packed will result in a nonlinear increase of elastic modulus as a function of V_f.

CONCLUSIONS

In summary, we have applied energy filtered tomography image acquisition and developed improved analysis methods for the study of CNT−polymer nanocomposites. The techniques detailed here are also applicable to other low-contrast nanocomposites. The superior quality of the tomographic reconstructions permits a rich, quantitative data set to be extracted, including accurate measures of V_f and alignment, bundle/network topology, and detailed 3D waviness characterization. For the samples examined here, our measurements explain the nonlinear dependence of some material properties on CNT volume fraction. The 3D TEM tomographic data provide an essential component that enables the development of multiscale models that link atomistic and continuum models of CNT−polymer nanocomposites. More broadly, data of this type will lead to a quantitative understanding of the gap between the expected and measured properties of CNT-based nanocomposites and will aid in the development of optimized processing methods that allow the full potential of these exciting multifunctional materials to be realized.

METHODS

Carbon Nanotube (CNT) Growth and Nanocomposite (PNC) Processing. CNT growth,[53] densification and impregnation have been detailed in previous work.[6,10] Briefly, CNTs were grown using thermal chemical vapor deposition (CVD). Thin catalyst layers of Fe/Al$_2$O$_3$ were deposited on 1 cm × 1 cm silicon wafers. CVD was performed at (800 ± 20) °C, at atmospheric pressure, using C$_2$H$_4$, H$_2$, and He (bubbled through water, (500 ± 200) μL/L water vapor during the growth) reactant gases. This process results in a well-aligned forest of 1 mm long CNTs with a volume fraction (V_f) of 1% (density of 10^9 to 10^{10} CNTs cm^{-2}). The as-grown CNT forests were then released from the wafer, and compressed using a mechanical biaxial densification instrument to the desired nominal V_f (1%, 5%, 6%, and 11.7%, estimated from the change in area of the compressed forests before impregnation). The compressed forests were placed in a mold, and an aerospace-grade epoxy, of viscosity ≈80 mPa·s at 90 °C was poured into the mold. The forest is infiltrated by the epoxy through capillary action. The PNC was then cured following the manufacturer-recommended procedure: 1 h at 160 °C and 2 h at 180 °C. It should be noted that, as part of the conclusions drawn from this study, the CNT forest expands during impregnation, and so the measured values of V_f [(0.44 ± 0.007) %, (2.58 ± 0.25) %, (4.04 ± 0.19) %, and (6.89 ± 0.43) %] are significantly smaller than the nominal ones.

TEM Sample Preparation. The top and bottom surfaces of the PNC along the CNT alignment direction were polished to remove the unaligned top surface crust and bottom layer. The other exposed surfaces of the samples were polished to remove any residual neat epoxy, which ensured that the sample was grounded when mounted on an SEM stub owing to the high conductivity of the CNTs. A 3 μm thick protective Pt cap of size 15 μm × 2 μm was ion-beam deposited on the sample surface. A 30 kV, 9.3 nA Ga$^+$ ion beam was used to mill trenches around the protected area and a 10 μm deep region directly under the platinum was lifted out and mounted on a half grid using ion beam deposited platinum. The mounted sample (of approximate size 15 μm × 2 μm × 10 μm) was further thinned to a lamella (of approximate size 200 nm × 10 μm × 15 μm) using a 30 kV, 0.24 nA Ga$^+$ ion beam (Supporting Information Figure S1c). Final cleaning of the lamella surface was performed at 5 kV and 18 pA. The TEM sample was then dipped into a solution of 5 nm gold particles in deionized water and dried under a heat lamp for 1 h (Supporting Information Figure S1d). Ultramicrotomy, traditionally employed for TEM sample preparation in nanocomposites, was not used as it leads to CNT pullout and false alignment,[54] which interferes with any CNT directionality analysis.

TEM Imaging. FIB prepared samples were imaged by BF-TEM at 300 kV with a 40 μm objective aperture inserted. A 10 eV wide slit was centered about the zero-loss peak of the energy spectrum in order to enhance the contrast between the CNT and the matrix epoxy. The fields of view varied between 1350 nm × 1350 and 896 nm × 896 nm. Tilt series were acquired between −60° and +60°, at intervals of 2°, with 2 s exposure times, at a resolution of 2048 pixels × 2048 pixels. A typical dose of 10^6 electrons/nm^2 (10^4 electrons/Å^2) was used per image. Manual tracking of the gold particles was performed during acquisition in order ensure that the field of view remained centered.

Reconstruction. The tilt series was further aligned to subpixel accuracy using gold bead tracking (using 5 gold particles per tilt series). Tilt axis alignments were performed to minimize reconstruction artifacts. Reconstructions were performed using 50 iterations of the Simultaneous Iterative Reconstruction Technique (SIRT) algorithm. The output files were converted into a stack of TIF images for segmentation on ImageJ. Three samples, prepared from random locations on the bulk material, were imaged, reconstructed and visualized for every V_f in order to ensure statistical relevance and sample uniformity. The characterization of such a large number of samples is facilitated by the fast segmentation methodology developed here. This segmentation method reduces the average time required for tomography from 7 working days (manual segmentation) to 3 h. The uniformity of CNT density was additionally confirmed using (30 μm × 30 μm) conducting-AFM images (Supporting Information Figure S2) and (99 μm × 84 μm) Raman scattering maps of microtomed slices (Supporting Information Figure S3), both of which indicate that there is no micrometer-scale (or larger) phase separation between the CNT and polymer phases. Although we do not observe voids in these systems, we note that our methodology is well-suited for the quantification of the volume fractions of nanoscale voids.

REFERENCES AND NOTES

1. Pandey, G.; Thostenson, E. T. Carbon Nanotube-Based Multifunctional Polymer Nanocomposites. *Polym. Rev.* **2012**, *52*, 355–416.

2. Thostenson, E. T.; Chou, T.-W. Processing-Structure-Multi-Functional Property Relationship in Carbon Nanotube/ Epoxy Composites. *Carbon* **2006**, *44*, 3022–3029.

3. Balazs, A. C.; Emrick, T.; Russell, T. P. Nanoparticle Polymer Composites: Where Two Small Worlds Meet. *Science* **2006**, *314*, 1107–1110.

4. Vaddiraju, S.; Cebeci, H.; Gleason, K. K.; Wardle, B. L. Hierarchical Multifunctional Composites by Conformally Coating Aligned Carbon Nanotube Arrays with Conducting Polymer. *ACS Appl. Mater. Interfaces* **2009**, *1*, 2565–2572.

5. Fu, K.; Yildiz, O.; Bhanushali, H.; Wang, Y.; Stano, K.; Xue, L.; Zhang, X.; Bradford, P. D. Aligned Carbon Nanotube-Silicon Sheets: A Novel Nano-Architecture for Flexible Lithium Ion Battery Electrodes. *Adv. Mater.* **2013**, *25*, 5109–5114.

6. Cebeci, H.; Villoria, R. G. de; Hart, A. J.; Wardle, B. L. Multi-functional Properties of High Volume Fraction Aligned Carbon Nanotube Polymer Composites with Controlled Morphology. *Compos. Sci. Technol.* **2009**, *69*, 2649–2656.

7. Vigolo, B. Macroscopic Fibers and Ribbons of Oriented Carbon Nanotubes. *Science* **2000**, *290*, 1331–1334.

8. Koziol, K.; Vilatela, J.; Moisala, A.; Motta, M.; Cunniff, P.; Sennett, M.; Windle, A. High-Performance Carbon Nanotube Fiber. *Science* **2007**, *318*, 1892–1895.

9. Gonnet, P.; Liang, Z.; Choi, E. S.; Kadambala, R. S.; Zhang, C.; Brooks, J. S.; Wang, B.; Kramer, L. Thermal Conductivity of Magnetically Aligned Carbon Nanotube Buckypapers and Nanocomposites. *Curr. Appl. Phys.* **2006**, *6*, 119–122.

10. Wardle, B. L.; Saito, D. S.; Garcia, E. J.; Hart, A. J.; de Villoria, R. G.; Verploegen, E. A. Fabrication and Characterization of Ultrahigh-Volume-Fraction Aligned Carbon Nanotube-Polymer Composites. *Adv. Mater.* **2008**, *20*, 2707–2714.

11. Thostenson, E. T.; Chou, T.-W. Aligned Multi-Walled Carbon Nanotube-Reinforced Composites: Processing and Mechanical Characterization. *J. Phys. Appl. Phys.* **2002**, *35*, L77–L80.

12. García, E. J.; Hart, A. J.; Wardle, B. L.; Slocum, A. H. Fabrication and Nanocompression Testing of Aligned Carbon-Nanotube−Polymer Composites. *Adv. Mater.* **2007**, *19*, 2151–2156.

13. Huang, H.; Liu, C. H.; Wu, Y.; Fan, S. Aligned Carbon Nanotube Composite Films for Thermal Management. *Adv. Mater.* **2005**, *17*, 1652–1656.

14. Futaba, D. N.; Hata, K.; Yamada, T.; Hiraoka, T.; Hayamizu, Y.; Kakudate, Y.; Tanaike, O.; Hatori, H.; Yumura, M.; Iijima, S. Shape-Engineerable and Highly Densely Packed Single-Walled Carbon Nanotubes and Their Application as Super-Capacitor Electrodes. *Nat. Mater.* **2006**, *5*, 987–994.

15. Lachman, N.; Xu, H.; Zhou, Y.; Ghaffari, M.; Lin, M.; Bhattacharyya, D.; Ugur, A.; Gleason, K. K.; Zhang, Q. M.; Wardle, B. L. Tailoring Thickness of Conformal Conducting Polymer Decorated Aligned Carbon Nanotube Electrodes for Energy Storage. *Adv. Mater. Interfaces* **2014**, *1*, 1400076.

16. Hinds, B. J.; Chopra, N.; Rantell, T.; Andrews, R.; Gavalas, V.; Bachas, L. G. Aligned Multiwalled Carbon Nanotube Membranes. *Science* **2004**, *303*, 62–65.

17. Marconnet, A. M.; Yamamoto, N.; Panzer, M. A.; Wardle, B. L.; Goodson, K. E. Thermal Conduction in Aligned Carbon Nanotube−Polymer Nanocomposites with High Packing Density. *ACS Nano* **2011**, *5*, 4818–4825.

18. Fisher, F. T.; Bradshaw, R. D.; Brinson, L. C. Effects of Nanotube Waviness on the Modulus of Nanotube-Reinforced Polymers. *Appl. Phys. Lett.* **2002**, *80*, 4647–4649.

19. Herasati, S.; Zhang, L. A New Method for Characterizing and Modeling the Waviness and Alignment of Carbon Nanotubes in Composites. *Compos. Sci. Technol.* **2014**, *100*, 136–142.

20. García, E. J.; Hart, A. J.; Wardle, B. L.; Slocum, A. H. Fabrication of Composite Microstructures by Capillarity-Driven Wetting of Aligned Carbon Nanotubes with Polymers. *Nanotechnology* **2007**, *18*, 165602.

21. Stein, I. Y.; Wardle, B. L. Morphology and Processing of Aligned Carbon Nanotube Carbon Matrix Nanocomposites. *Carbon* **2014**, *68*, 807–813.

22. Jinnai, H.; Spontak, R. J.; Nishi, T. Transmission Electron Microtomography and Polymer Nanostructures. *Macromolecules* **2010**, *43*, 1675–1688.

23. Ma, H.-Y.; Tong, L.-F.; Xu, Z.-B.; Fang, Z.-P. Functionalizing Carbon Nanotubes by Grafting on Intumescent Flame Retardant: Nanocomposite Synthesis, Morphology, Rheology, and Flammability. *Adv. Funct. Mater.* **2008**, *18*, 414–421.

24. Gojny, F. H.; Wichmann, M. H. G.; Fiedler, B.; Kinloch, I. A.; Bauhofer, W.; Windle, A. H.; Schulte, K. Evaluation and Identification of Electrical and Thermal Conduction Mechanisms in Carbon Nanotube/Epoxy Composites. *Polymer* **2006**, *47*, 2036–2045.

25. Midgley, P. A.; Dunin-Borkowski, R. E. Electron Tomography and Holography in Materials Science. *Nat. Mater.* **2009**, *8*, 271–280.

26. Van Tendeloo, G.; Bals, S.; Van Aert, S.; Verbeeck, J.; Van Dyck, D. Advanced Electron Microscopy for Advanced Materials. *Adv. Mater.* **2012**, *24*, 5655–5675.

27. Hindson, J. C.; Saghi, Z.; Hernandez-Garrido, J. C.; Midgley, P. A.; Greenham, N. C. Morphological Study of Nanoparticle-Polymer Solar Cells Using High-Angle Annular Dark-Field Electron Tomography. *Nano Lett.* **2011**, *11*, 904–909.

28. Kohjiya, S.; Katoh, A.; Shimanuki, J.; Hasegawa, T.; Ikeda, Y. Three-Dimensional Nano-Structure of *in Situ* Silica in Natural Rubber as Revealed by 3D-TEM/Electron Tomography. *Polymer* **2005**, *46*, 4440–4446.

29. Drummy, L. F.; Wang, Y. C.; Schoenmakers, R.; May, K.; Jackson, M.; Koerner, H.; Farmer, B. L.; Mauryama, B.; Vaia, R. A. Morphology of Layered Silicate-(Nanoclay-) Polymer Nanocomposites by Electron Tomography and Small-Angle X-Ray Scattering. *Macromolecules* **2008**, *41*, 2135–2143.

30. Loos, J.; Sourty, E.; Lu, K.; Freitag, B.; Tang, D.; Wall, D. Electron Tomography on Micrometer-Thick Specimens with Nanometer Resolution. *Nano Lett.* **2009**, *9*, 1704–1708.

31. Loos, J.; Alexeev, A.; Grossiord, N.; Koning, C. E.; Regev, O. Visualization of Single-Wall Carbon Nanotube (SWNT) Networks in Conductive Polystyrene Nanocomposites by Charge Contrast Imaging. *Ultramicroscopy* **2005**, *104*, 160–167.

32. Jinnai, H.; Spontak, R. J. Transmission Electron Microtomography in Polymer Research. *Polymer* **2009**, *50*, 1067–1087.

33. Reimer, L. Energy-Filtering Transmission Electron Microscopy. *Adv. Electron. Electron Phys.* **1991**, *81*, 43–126.

34. Grimm, R.; Typke, D.; Baumeister, W. Improving Image Quality by Zero-Loss Energy Filtering: Quantitative Assessment by Means of Image Cross-Correlation. *J. Microsc.* **1998**, *190*, 339–349.

35. Reimer, L.; Fromm, I.; Rennekamp, R. Operation Modes of Electron Spectroscopic Imaging and Electron Energy-Loss Spectroscopy in a Transmission Electron Microscope. *Ultramicroscopy* **1988**, *24*, 339–354.

36. Chen, D.; Goris, B.; Bleichrodt, F.; Mezerji, H. H.; Bals, S.; Batenburg, K. J.; de With, G.; Friedrich, H. The Properties of SIRT, TVM, and DART for 3D Imaging of Tubular Domains in Nanocomposite Thin-Films and Sections. *Ultramicroscopy* **2014**, *147C*, 137–148.

37. Frangakis, A. S.; Hegerl, R. Segmentation of Three-Dimensional Electron Tomographic Images. In *Electron Tomography*; Frank, J., Ed.; Springer: New York, 2006; pp 353−370.

38. Biermans, E.; Molina, L.; Batenburg, K. J.; Bals, S.; Van Tendeloo, G. Measuring Porosity at the Nanoscale by Quantitative Electron Tomography. *Nano Lett.* **2010**, *10*, 5014–5019.

39. Schneider, C. A.; Rasband, W. S.; Eliceiri, K. W. NIH Image to ImageJ: 25 Years of Image Analysis. *Nat. Methods* **2012**, *9*, 671–675.

40. Perona, P.; Malik, J. Scale-Space and Edge Detection Using Anisotropic Diffusion. *IEEE Trans. Pattern Anal. Mach. Intell.* **1990**, *12*, 629–639.

41. Wang, X. Y.; Lockwood, R.; Malac, M.; Furukawa, H.; Li, P.; Meldrum, A. Reconstruction and Visualization of Nanoparticle Composites by Transmission Electron Tomography. *Ultramicroscopy* **2012**, *113*, 96–105.

42. Midgley, P. A.; Weyland, M. 3D Electron Microscopy in the Physical Sciences: The Development of Z-Contrast and EFTEM Tomography. *Ultramicroscopy* **2003**, *96*, 413–431.

43. Kawase, N.; Kato, M.; Nishioka, H.; Jinnai, H. Transmission Electron Microtomography without the "Missing Wedge" for Quantitative Structural Analysis. *Ultramicroscopy* **2007**, *107*, 8–15.

44. Won, Y.; Gao, Y.; Panzer, M. A.; Xiang, R.; Maruyama, S.; Kenny, T. W.; Cai, W.; Goodson, K. E. Zipping, Entanglement, and the Elastic Modulus of Aligned Single-Walled Carbon Nanotube Films. *Proc. Natl. Acad. Sci. U.S.A.* **2013**, *110*, 20426–20430.

45. Coleman, J. N.; Khan, U.; Blau, W. J.; Gun'ko, Y. K. Small but Strong: A Review of the Mechanical Properties of Carbon Nanotube−Polymer Composites. *Carbon* **2006**, *44*, 1624–1652.

46. Doube, M.; Kłosowski, M. M.; Arganda-Carreras, I.; Cordelières, F. P.; Dougherty, R. P.; Jackson, J. S.; Schmid, B.; Hutchinson, J. R.; Shefelbine, S. J. BoneJ: Free and Extensible Bone Image Analysis in ImageJ. *Bone* **2010**, *47*, 1076–1079.

47. Arganda-Carreras, I.; Fernández-González, R.; Muñoz-Barrutia, A.; Ortiz-De-Solorzano, C. 3D Reconstruction of Histological Sections: Application to Mammary Gland Tissue. *Microsc. Res. Technol.* **2010**, *73*, 1019–1029.

48. Rezakhaniha, R.; Agianniotis, A.; Schrauwen, J. T. C.; Griffa, A.; Sage, D.; Bouten, C. V. C.; Van de Vosse, F. N.; Unser, M.; Stergiopulos, N. Experimental Investigation of Collagen Waviness and Orientation in the Arterial Adventitia Using Confocal Laser Scanning Microscopy. *Biomech. Model. Mechanobiol.* **2012**, *11*, 461–473.

49. Panzer, M. A.; Duong, H. M.; Okawa, J.; Shiomi, J.; Wardle, B. L.; Maruyama, S.; Goodson, K. E. Temperature-Dependent Phonon Conduction and Nanotube Engagement in Metalized Single Wall Carbon Nanotube Films. *Nano Lett.* **2010**, *10*, 2395–2400.

50. Fisher, F. T.; Bradshaw, R. D.; Brinson, L. C. Fiber Waviness in Nanotube-Reinforced Polymer Composites—I: Modulus Predictions Using Effective Nanotube Properties. *Compos. Sci. Technol.* **2003**, *63*, 1689–1703.

51. Cebeci, H.; Guzman de Villoria, R.; Jones, R.; Schulte, K.; Turkmen, H.; Wardle, B. In *Effective Stiffness of Wavy Aligned Carbon Nanotubes for Modeling of Controlled-Morphology Polymer Nanocomposites*; 53rd AIAA/ASME/ASCE/AHS/ASC Structures, Structural Dynamics and Materials Conference 20th AIAA/ASME/AHS, Honolulu, HI, 23−26 April, 2012; American Institute of Aeronautics and Astronautics: Reston, VA, 2012.

52. Handlin, D.; Stein, I. Y.; de Villoria, R. G.; Cebeci, H.; Parsons, E. M.; Socrate, S.; Scotti, S.; Wardle, B. L. Three-Dimensional Elastic Constitutive Relations of Aligned Carbon Nanotube Architectures. *J. Appl. Phys.* **2013**, *114*, 224310.

53. Hart, A. J.; Slocum, A. H. Rapid Growth and Flow-Mediated Nucleation of Millimeter-Scale Aligned Carbon Nanotube Structures from a Thin-Film Catalyst. *J. Phys. Chem. B* **2006**, *110*, 8250–8257.

54. Ajayan, P. M.; Stephan, O.; Colliex, C.; Trauth, D. Aligned Carbon Nanotube Arrays Formed by Cutting a Polymer Resin—Nanotube Composite. *Science* **1994**, *265*, 1212–1214.